

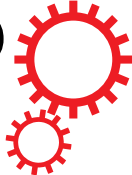


Title	A transparent electrochromic metal-insulator switching device with three-terminal transistor geometry
Author(s)	Katase, Takayoshi; Onozato, Takaki; Hirono, Misako; Mizuno, Taku; Ohta, Hiromichi
Citation	Scientific reports, 6, 25819 <a href="https://doi.org/10.1038/srep25819">https://doi.org/10.1038/srep25819</a>
Issue Date	2016-05-13
Doc URL	<a href="http://hdl.handle.net/2115/62263">http://hdl.handle.net/2115/62263</a>
Rights(URL)	<a href="http://creativecommons.org/licenses/by/4.0/">http://creativecommons.org/licenses/by/4.0/</a>
Type	article
File Information	srep25819.pdf



[Instructions for use](#)

# SCIENTIFIC REPORTS



OPEN

## A transparent electrochromic metal-insulator switching device with three-terminal transistor geometry

Received: 05 February 2016

Accepted: 22 April 2016

Published: 13 May 2016

Takayoshi Katase<sup>1</sup>, Takaki Onozato<sup>2</sup>, Misako Hirono<sup>3</sup>, Taku Mizuno<sup>4</sup> & Hiromichi Ohta<sup>1</sup>

Proton and hydroxyl ion play an essential role for tuning functionality of oxides because their electronic state can be controlled by modifying oxygen off-stoichiometry and/or protonation. Tungsten trioxide ( $\text{WO}_3$ ), a well-known electrochromic (EC) material for smart window, is a wide bandgap insulator, whereas it becomes a metallic conductor  $\text{H}_x\text{WO}_3$  by protonation. Although one can utilize electrochromism together with metal-insulator (MI) switching for one device, such EC-MI switching cannot be utilized in current EC devices because of their two-terminal structure with parallel-plate configuration. Here we demonstrate a transparent EC-MI switchable device with three-terminal TFT-type structure using amorphous (a-)  $\text{WO}_3$  channel layer, which was fabricated on glass substrate at room temperature. We used water-infiltrated nano-porous glass, CAN (calcium aluminate with nanopores), as a liquid-leakage-free solid gate insulator. At virgin state, the device was fully transparent in the visible-light region. For positive gate voltage, the active channel became dark blue, and electrical resistivity of the a- $\text{WO}_3$  layer drastically decreased with protonation. For negative gate voltage, deprotonation occurred and the active channel returned to transparent insulator. Good cycleability of the present transparent EC-MI switching device would have potential for the development of advanced smart windows.

A transparent electrochromic metal-insulator (EC-MI) switching device that can be electrically switched from a colorless transparent insulator to a colored metallic conductor would be ideal for use in future energy-saving technologies, such as advanced smart-windows. In the OFF state such transparent EC-MI switching device fully transmits visible light, whereas in the ON state it does not transmit light. Furthermore, the device is switched from insulator to conductor at the same time, which can function as an ON/OFF power switch for other electronic devices.

Among many potential electrochromic materials, tungsten trioxide ( $\text{WO}_3$ )<sup>1</sup> shows the greatest suitability for the EC-MI switching devices. Stoichiometric  $\text{WO}_3$  is a transparent insulator with a bandgap ( $E_g$ ) of 2.6–3.0 eV<sup>2</sup> and has a defect perovskite-type structure with space group  $P2_1/n$ , in which A-sites in the  $\text{ABO}_3$  lattices are vacant<sup>3</sup>. If the vacant A-sites become occupied by protons ( $\text{H}^+$ ), i.e. the formation of tungsten bronze, it becomes an electrical conductor and opaque to visible light following the valence-state change of W ion from  $\text{W}^{6+}$  to  $\text{W}^{5+4}$ . Thus, the protonation/deprotonation of  $\text{WO}_3$  is promising for the realization of simultaneous electrical switching between colorless/colored and insulating/conducting states, as shown in Fig. 1.

Various types of  $\text{WO}_3$ -based EC devices have been actively developed for applications in energy-saving smart windows<sup>5,6</sup>; however, their MI switching behavior has not been utilized with EC switching simultaneously, because of their two-terminal structure, which involves a parallel-plate electrode configuration. Electrostatic charge modulation using three-terminal thin-film transistors (TFTs)<sup>7,8</sup> on a  $\text{WO}_3$  thin film could be used to realize simultaneous EC-MI switching; however, it remains difficult to fully switch their coloring state, because of

<sup>1</sup>Research Institute for Electronic Science, Hokkaido University, N20W10, Kita, Sapporo 001–0020, Japan.

<sup>2</sup>Graduate School of Information Science and Technology, Hokkaido University, N14W19, Kita, Sapporo 060–0814, Japan. <sup>3</sup>School of Engineering, Hokkaido University, N13W8, Kita, Sapporo 060–8628, Japan. <sup>4</sup>Graduate School of Engineering, Nagoya University, Furo-cho, Chikusa, Nagoya 464–8603, Japan. Correspondence and requests for materials should be addressed to T.K. (email: katase@es.hokudai.ac.jp) or H.O. (email: hiromichi.ohta@es.hokudai.ac.jp)

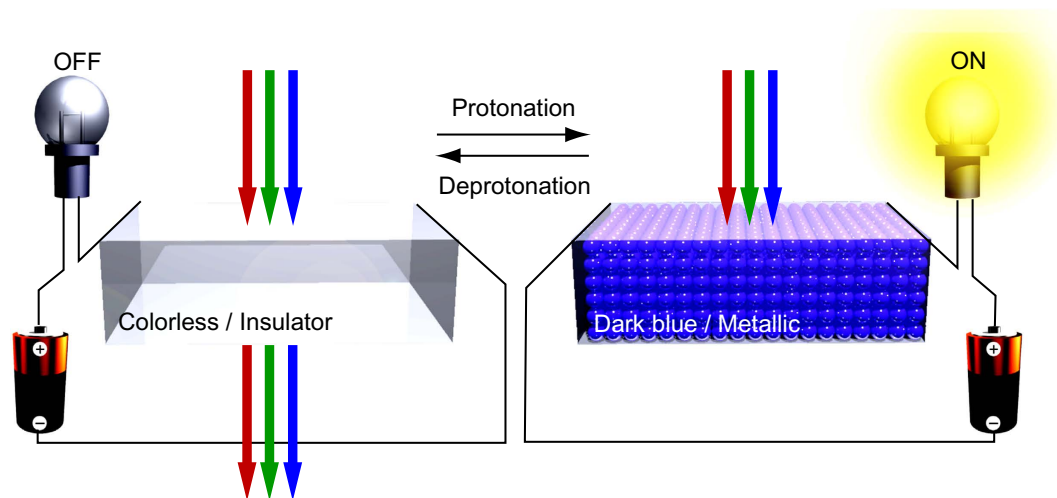


**Figure 1.** Concept of an electrochromic metal-insulator switching device. The device can be switched from a colorless transparent/insulator state to a dark blue/metallic state simultaneously by electrochemical protonation/deprotonation at RT in air. In the ON state, the visible light cannot be transmitted through the device, whereas it can be fully transmitted in the OFF state. Further, the device can function as an ON/OFF power switch for other electronic devices at the same time. Such a device would be useful for advanced smart window application.

limitations associated with the carrier-doping range and modifiable thickness<sup>9</sup>. Several researchers have developed liquid-electrolyte gated transistors<sup>10,11</sup> and successfully demonstrated EC-MI switching of  $\text{WO}_3$ . However, because these devices require liquid electrolytes, they are less practical for application, which depends on effective sealing.

Herein, we demonstrate a *liquid-leakage-free* transparent EC-MI switching device. Figure 2a schematically illustrates the device structure, which has a typical three-terminal TFT- geometry composed of an active channel, a gate insulator, and source-drain-gate electrodes. We used an amorphous (a-)  $\text{WO}_3$  thin film as the active channel layer, because EC switching of a- $\text{WO}_3$  film prepared on glass substrate at room temperature (RT) has been previously reported<sup>12</sup>. The gate insulator consists of an a- $12\text{CaO}\cdot 7\text{Al}_2\text{O}_3$  (a-C12A7) thin film with nanoporous structure (calcium aluminate with nanopore, CAN)<sup>13,14</sup>. It should be noted that the film porosity of CAN film can be controlled by oxygen pressure ( $P_{\text{O}_2}$ ) during thin-film deposition at RT (porous structure can be observed at  $P_{\text{O}_2} > 1$  Pa), and the nanopores with average diameters of 10–20 nm connect with each other, when the porosity reaches ~30% of fully dense film, leading to the percolation conduction of water in the CAN film. Since C12A7 is a hygroscopic material, water vapor in air is automatically absorbed into the CAN film, like a solid sponge, via the capillary action in the interconnected nanopores. Therefore, water electrolysis can be used in the solid gate insulator. A NiO/ITO (indium tin oxide) bilayer film was used as the gate transparent electrode, and ITO thin films were used as the transparent source and drain electrodes.

The device with leakage-free water can be considered as the nanosized electrochemical cell with a nanogap parallel plate structure, which enables the high electric-field application for ion migration and effective protonation/deprotonation of the a- $\text{WO}_3$  layer (Fig. 2b). Thus, a gate voltage ( $V_g$ ) application induces water electrolysis in the CAN film, and produced  $\text{H}^+$  and  $\text{OH}^-$  ions move to protonate the a- $\text{WO}_3$  layer ( $\text{WO}_3 + x\text{H}^+ + xe^- \rightarrow \text{H}_x\text{WO}_3$ )<sup>15</sup> and hydroxylate the NiO layer ( $\text{NiO} + \text{OH}^- \rightarrow \text{NiOOH} + e^-$ )<sup>16</sup>, respectively. The NiO counter layer is expected to work as the  $\text{OH}^-$  absorber, which maintains a better electrochemical balance and should improve the reversibility and reproducibility of device operation. Alternative positive and negative  $V_g$  applications induce the reversible protonation/deprotonation of a- $\text{WO}_3$  layer, switching it from a transparent insulator to a dark blue conductor. The present EC-MI switching device with the two combined functions of color changing as a display and electrical switching as a transistor in one device can be reversibly operated at RT without sealing; thus, it may be suitable for a wide-range application in future energy-saving technologies, such as advanced smart-windows.

## Results

**Device fabrication.** The EC-MI switching device was fabricated on an alkaline-free glass substrate (Corning® EAGLE XG®) by using stencil masks. All the thin-film fabrication processes were conducted at RT using pulsed laser deposition (PLD) with KrF excimer laser ( $\lambda = 248$  nm). Details of the device fabrication process are provided in experimental section. First, 20-nm-thick transparent conducting ITO films (resistivity,  $\rho = 1.0$  m $\Omega$  cm at RT) were deposited as source and drain electrodes. An 80-nm-thick a- $\text{WO}_3$  channel film, a 300-nm-thick CAN gate insulator film<sup>13,14</sup>, and a NiO (20 nm)/ITO (20 nm) gate electrode film were then deposited in turn. The channel size was 800  $\mu\text{m} \times$  400  $\mu\text{m}$ . The density of a- $\text{WO}_3$  film was 5.96 g cm<sup>-3</sup>, evaluated by grazing incidence X-ray reflectivity, which corresponds to 82% of ideal density of a  $\text{WO}_3$  crystal (7.29 g cm<sup>-3</sup>)<sup>17</sup>. The AC conductivity of the CAN film was 3.7  $\times 10^{-8}$  S cm<sup>-1</sup> at RT, slightly less than the 5.6  $\times 10^{-8}$  S cm<sup>-1</sup> of ultrapure water<sup>18</sup>.

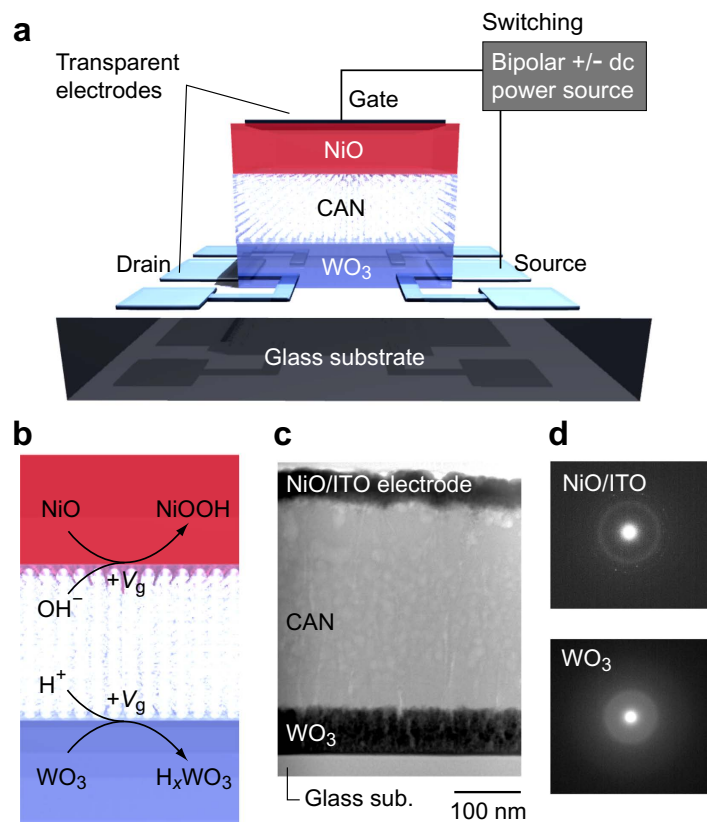


**Figure 2. A transparent EC-MI switching device.** (a) Schematic device structure of three-terminal TFT-type device, composed of a- $\text{WO}_3$  (80 nm), CAN (300 nm), and NiO (20 nm)/ITO (20 nm) layers. Transparent ITO thin films are used for all the electrodes. (b) Device operation mechanism. During the positive  $V_g$  application, protonation of a- $\text{WO}_3$  layer and hydroxylation of NiO layer occur simultaneously. Conversely, a- $\text{H}_x\text{WO}_3$  and NiOOH return to a- $\text{WO}_3$  and NiO during the negative  $V_g$  application. (c) Cross-sectional BF-STEM image of the device. Trilayer structure is clearly seen. Many light spots in the CAN layer indicate nanopores, which is fully occupied with water. (d) Selected area electron diffraction patterns of NiO/ITO layer (upper) and a- $\text{WO}_3$  layer (lower).

Figure 2c shows a bright-field scanning transmission electron microscopy (BF-STEM, in which heavier atoms appear darker) image of the cross-section of the resultant device, which reveals the multi-layer structure of ITO (20 nm)/NiO (20 nm)/CAN (300 nm)/a- $\text{WO}_3$  (80 nm) on a glass substrate. Numerous light spots with diameters of 10–20 nm are clearly seen in the CAN film, indicating the presence of high-density nanopores in the CAN film. Figure 2d summarizes the selected-area electron diffraction patterns of the NiO/ITO gate electrode layer (upper) and the a- $\text{WO}_3$  channel layer (bottom). A broad halo was observed for the a- $\text{WO}_3$  film, confirming the amorphous structure. Meanwhile, a ring diffraction pattern was seen for NiO/ITO film, originating from polycrystalline nature of NiO film, which was also confirmed by the grazing incidence X-ray diffraction measurements on each thin film.

**Metal-insulator switching.** We first evaluated the MI switching of the device by measuring sheet resistance ( $R_s$ ) and thermopower ( $S$ ) at RT, after applying and subsequently switching off  $V_g$ . Figure 3a plots  $R_s$  as a function of applied  $\pm V_g$  at RT. First, a positive  $V_g$  up to +10 V was applied to protonate the a- $\text{WO}_3$  channel (left panel, each  $V_g$  application time of 20 s), and then negative  $V_g$  up to -10 V was applied to deprotonate the a- $\text{H}_x\text{WO}_3$  channel (right panel, each  $V_g$  application time of 10 s). The initial a- $\text{WO}_3$  channel was highly insulating ( $R_s$  was not in measurable range), but the reduction in  $R_s$  of more than six orders of magnitude was observed by applying positive  $V_g$ ; the  $R_s$  exponentially decreased from  $17 \text{ M}\Omega \text{ sq.}^{-1}$  at +2 V and their saturation was observed at  $\geq +8 \text{ V}$ , where the  $R_s$  reached to  $30 \Omega \text{ sq.}^{-1}$  at +10 V. It should be noted that the protonated a- $\text{H}_x\text{WO}_3$  channel was stable under ambient and vacuum conditions at RT after the + $V_g$  application, confirming the non-volatility of device operation due to the electrochemical reaction. Subsequently, by applying negative  $V_g$  up to -10 V,  $R_s$  clearly recovered, reaching an insulating state ( $6.8 \text{ M}\Omega \text{ sq.}^{-1}$ ).

We then measured the  $S$  for a- $\text{WO}_3$  channel protonated and deprotonated at each  $\pm V_g$ , because  $S$  is a good measure to evaluate the electronic-structure change resulting from carrier doping (protonation)<sup>19,20</sup>. Figure 3b shows the relationship between  $S$  and  $1/R_s$  for the device at RT.  $S$ -values were always negative, indicating that the channel layer is an n-type conductor. The  $|S|$  linearly decreased from  $47 \mu\text{V K}^{-1}$  to  $11 \mu\text{V K}^{-1}$  with logarithmic increase in  $1/R_s$  and the linear relation was reversibly observed with the application of  $\pm V_g$ , suggesting that

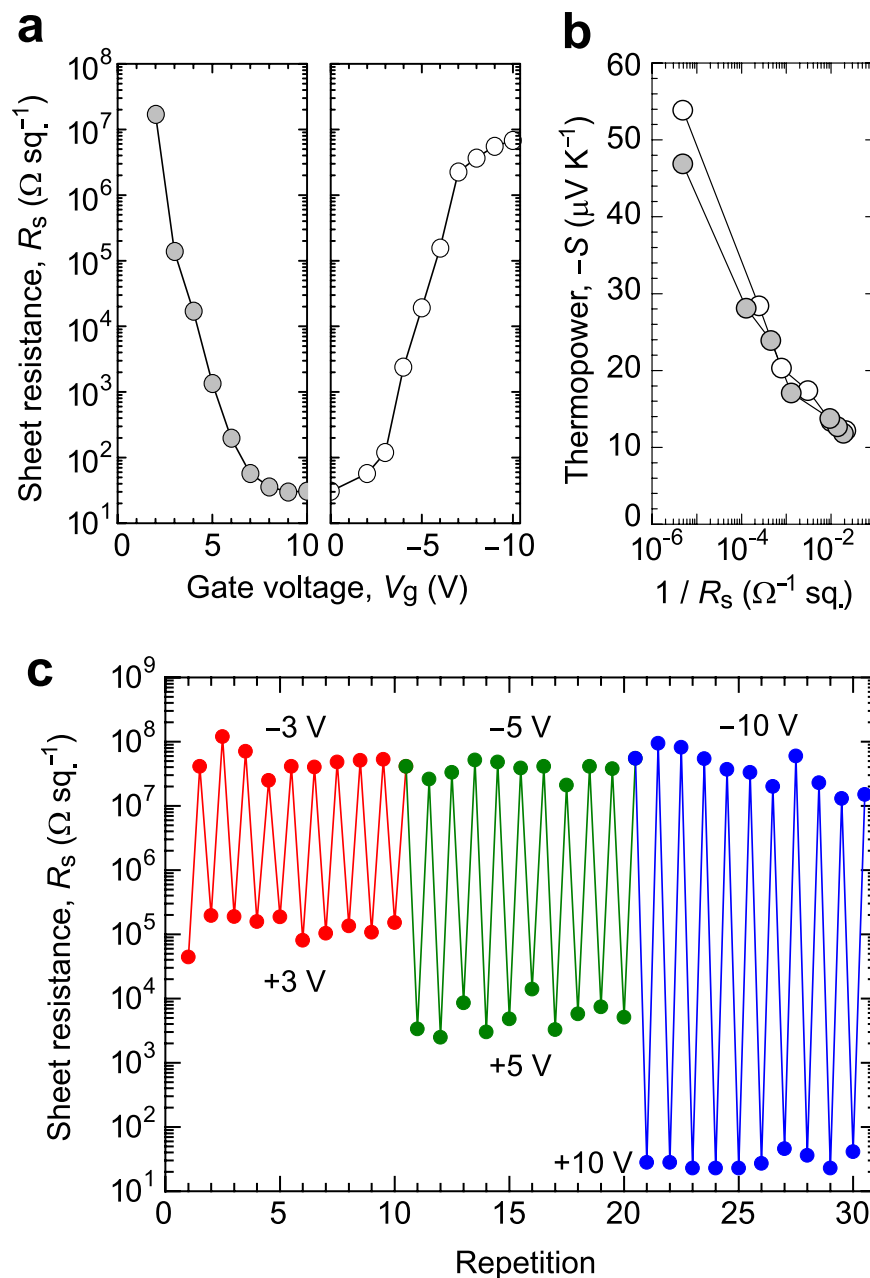


**Figure 3. Metal-insulator switching of the transparent EC-MI switching device.** (a) Sheet resistance ( $R_s$ ) as a function of applied  $V_g$  for a- $\text{WO}_3$  layer.  $R_s$  values were measured after  $V_g$  application, where positive  $V_g$  up to +10 V was applied for protonation of a- $\text{WO}_3$  film (left panel, each  $V_g$  application time of 20 s), and then negative  $V_g$  up to -10 V was applied for deprotonation of a- $\text{H}_x\text{WO}_3$  film (right panel, each  $V_g$  application time of 10 s). (b) Thermopower ( $S$ ) as a function of  $1/R_s$  at RT. The linear relation between  $-S$  and logarithmic  $1/R_s$  was reversibly observed by  $\pm V_g$  application. (c) Repetitive switching property by applying various  $V_g = \pm 3$ ,  $\pm 5$ , and  $\pm 10$  V. The  $R_s$  modulation ratio can be controlled to be  $\sim 10^3$  for  $\pm 3$  V,  $\sim 10^4$  for  $\pm 5$  V, and  $\sim 10^6$  for  $\pm 10$  V, respectively.

protonation of the a- $\text{WO}_3$  channel provides electrons to the conduction band, and the energy derivative of the electronic density of states (DOS) near the Fermi energy ( $E_F$ ),  $\left[ \frac{\partial \text{DOS}(E)}{\partial E} \right]_{E=E_F}$ , becomes moderate, resulting in the consequent reduction of  $|S|$ -values.

Figure 3c shows the results of repeated  $R_s$  switching of the a- $\text{WO}_3$  channel at various  $V_g$ , e.g.  $\pm 3$ ,  $\pm 5$ , and  $\pm 10$  V, where the  $V_g$  application time was 20 s for protonation ( $+V_g$ ) and 10 s for deprotonation ( $-V_g$ ). Clear cyclability of  $R_s$  switching was observed at each  $V_g$ , and the  $R_s$  modulation ratio was largely dependent on the applied  $V_g$ : the ON/OFF ratio was  $\sim 10^3$  at  $\pm 3$  V,  $\sim 10^4$  at  $\pm 5$  V, and  $\sim 10^6$  at  $\pm 10$  V. Reversible and reproducible  $R_s$  switching with large ON/OFF ratios occurred rapidly on the second-time scale.

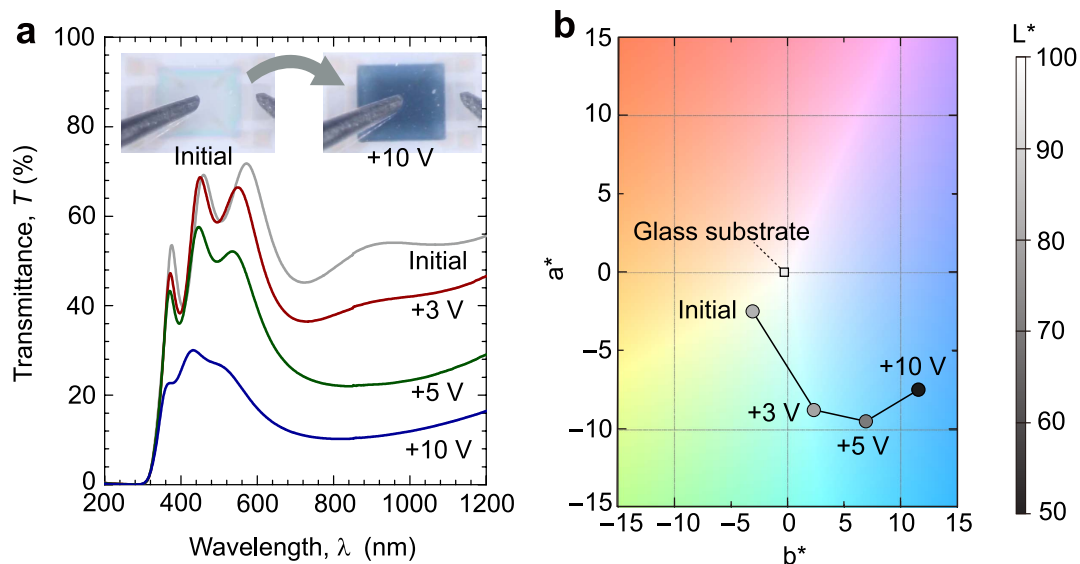


**Figure 4. Electrochromic switching of the transparent EC-MI switching device.** (a) Optical transmission spectra of the device. Significant decrease of the transmission is seen with increasing  $V_g$ . The inset shows the photographs of the device; after the application of  $V_g = +10$  V, the device became opaque/dark blue (right), whereas the device was colorless transparent at the initial state (left). (b)  $L^*a^*b^*$  color space plot of the device at each state in (a).

The device operation is considered to be largely dependent on the time-scaled processes consisted of ionic polarization in water, electric double layer formation, electrochemical reaction, and  $H^+$  diffusion in a- $WO_3$  channel under the  $V_g$  applications. The rate-determining step among them for the protonation of  $WO_3$  has been reported to be the surface reaction process<sup>21,22</sup>. Therefore, the difference of the application time of  $+V_g$  (protonation) and  $-V_g$  (deprotonation) should originate from the activation barrier for the surface reaction, i.e. the in-diffusion and out-diffusion of  $H^+$  transport have different interfacial resistances<sup>23</sup>, which can be seen in the different gate current flowing in the device even at the same  $\pm V_g$  (it will be shown later). In addition, the  $V_g$ -dependent ON/OFF ratio of the  $R_s$  modulation (Fig. 3c) suggests that the  $H^+$  diffuses from the surface and the penetration depth along the out-of-plane direction can be controlled by the  $V_g$ , where the entire channel region is protonated by applying  $V_g \geq 8$  V.

**Electrochromic switching.** We next evaluated the EC switching of the device. Figure 4a shows the optical transmission spectra of the device in the initial state (black line) and protonated states at +3 V (red line), +5 V (green line), and +10 V (blue line). The transmission ( $T$ ) of the device was largely changed by the applied  $+V_g$ . The initial device was, to some extent, transparent in the visible light region. After protonation,  $T$  at  $\lambda = 700$  nm reduced to 24% that of the initial state (transmission modulation of 35%). The inset shows the device picture at the initial and protonated states (+10 V); the color clearly changes from transparent colorless to opaque dark blue, as can be seen in  $L^*a^*b^*$  color space (Fig. 4b), reflecting the optical modulation of the a- $WO_3$  channel by RT protonation. Thus, simultaneous EC-MI switching was realized in the device. It should be noted that there is no direct evidence for the hydroxylation of NiO to make NiOOH in this device, which should also affect the optical transmission spectra; NiO changes its color from transparent to deep brown by hydroxylation<sup>24</sup>. However, considering that the no gas generation was confirmed in this device, which is indirect evidence to suggest the  $OH^-$  ion absorption in NiO counter layer, and there are many reports on the hydroxylation of NiO with aqueous solutions and their effect on electrochromic devices<sup>24</sup>, NiO should play as  $OH^-$  absorption layer but further confirmation is necessary.

## Discussion

To clarify the device operation mechanism, we investigated the relationship between the flowing current and  $R_s$  of the a- $WO_3$  channel under various  $V_g$  conditions. Figure 5a,b summarize the retention-time ( $t$ ) dependence of the gate current ( $I_g$ ) along with  $R_s$  for the a- $WO_3$  channel under  $\pm V_g$  values of 3, 5, and 10 V, where the  $+V_g$  was initially applied for protonation (Fig. 5a) and  $-V_g$  was subsequently applied for deprotonation (Fig. 5b).  $I_g$  and  $R_s$  were measured during and after the  $V_g$  application, respectively. Upon  $+V_g$  application (Fig. 5a),  $+I_g$  increased with  $t$  for all applied  $+V_g$  (the  $I_g$  at +10 V showed an irregular jump and exponentially increased and then exhibited the saturation at last), while  $R_s$  simultaneously decreased, indicating that electrochemical protonation of the a- $WO_3$  channel occurred. Meanwhile, upon  $-V_g$  application (Fig. 5b),  $-I_g$  decreased with  $t$  at each  $-V_g$  while  $R_s$  simultaneously increased due to electrochemical deprotonation. This observation suggests the following device operation mechanism. The  $+V_g$  application first accumulates charge carriers at film surface via electrostatic field effect with small  $+I_g$ , resulting in the formation of parallel-plate capacitor, i.e. the electric field starts to be well applied on the channel surface, and a further  $+V_g$  application generates dissociated  $H^+$  and  $OH^-$  ions and

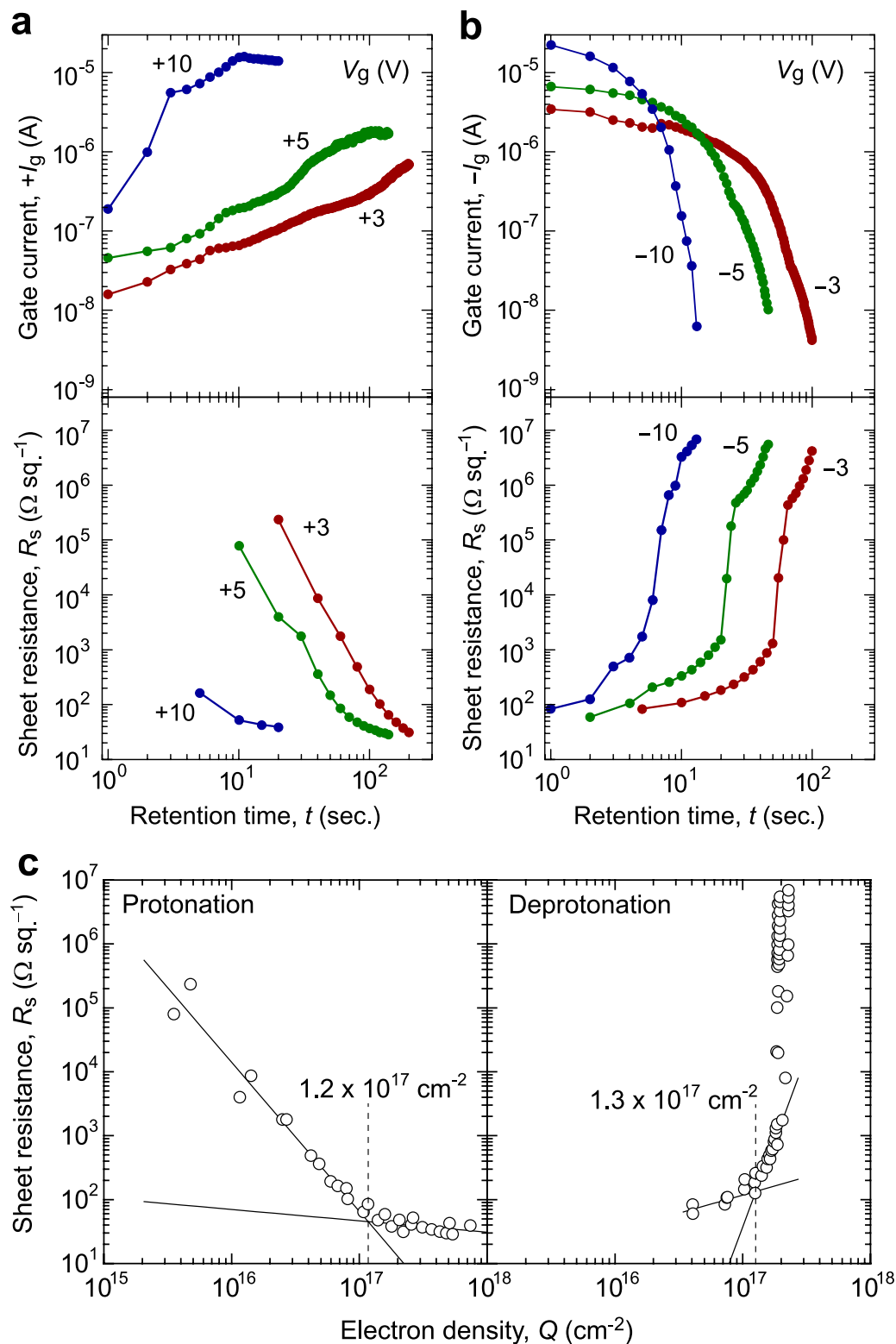


**Figure 5. Switching mechanism of the transparent EC-MI switching device.** (a,b) Retention time ( $t$ ) dependence of gate current ( $I_g$ , upper) and sheet resistance ( $R_s$ , lower) under application of various  $\pm V_g$ 's from 3, 5, and 10 V, where (a)  $+V_g$  was initially applied for protonation and (b)  $-V_g$  was subsequently applied for deprotonation. (c) Electron-density ( $Q$ ) dependence of  $R_s$  under application of the various  $V_g$ 's. The  $Q$  was calculated as the integrated value of the  $I_g$ - $t$  plots in (a,b). The universal changes in  $R_s$  are presented by the black lines. The critical  $Q$  of protonation and deprotonation was  $1.2$ – $1.3 \times 10^{17} \text{ cm}^{-2}$ , which corresponds well with the ideal  $Q$  ( $1.3 \times 10^{17} \text{ cm}^{-2}$ ) required for the 100% protonation/deprotonation reaction of  $\text{WO}_3 + \text{H}^+ + \text{e}^- \rightleftharpoons \text{HWO}_3$ .

attracted them to each film surface, which should be primary origin of the significant increase of  $I_g$  at the initial stage. The  $H^+$  and  $OH^-$  ions diffuse from the surface to bulk region of a- $WO_3$  film and NiO counter layer, where the improvement of conductivity of each layer exponentially increases the  $I_g$ .

We then compared the variation in  $R_s$  of the a- $WO_3$  channel with respect to applied electron density (Fig. 5c) estimated as  $Q = \frac{C}{S \times q}$ , where  $C$  is total coulomb amount calculated from the integral value of the  $I_g-t$  plots in Fig. 5a,b,  $S$  is the surface area of a- $WO_3$  channel, and  $q$  is elementary charge, respectively. For protonation ( $+V_g$  application),  $R_s$  steeply decreased with increasing  $Q$  up to  $1.2 \times 10^{17} \text{ cm}^{-2}$  ( $\equiv 1.5 \times 10^{22} \text{ cm}^{-3}$ ) and then kept unchanged with further electron injection. In contrast, for deprotonation ( $-V_g$  application),  $R_s$  increased moderately at  $Q$  up to  $1.3 \times 10^{17} \text{ cm}^{-2}$  ( $\equiv 1.6 \times 10^{22} \text{ cm}^{-3}$ ), after which it sharply switched to insulating state. The  $Q$  described here does not mean the carrier concentration in the film but electrochemically-used electron density ( $\approx H^+$  concentration). Referring to the previous report on  $H^+$  implantation<sup>25</sup>, almost the same dose density ( $\sim 10^{17} \text{ cm}^{-2}$ ) of  $H^+$  was used for metallization of  $WO_3$ , but the carrier concentration was measured to be  $7.2 \times 10^{20} \text{ cm}^{-3}$ , where the efficiency of carrier generation was only  $\sim 60\%$ ; this situation should be equivalent for the present result. The change of  $R_s$  with  $Q$  seems to occur differently by protonation and deprotonation processes, which should come from the inhomogeneous  $H^+$  distribution in a- $H_xWO_3$  channel along the out-of-plane direction and the  $H^+$ -concentration dependent activity (chemical potential) of  $H^+$  transport<sup>26</sup>. The critical  $Q$  of MI switching of the a- $WO_3$  channel corresponds with the ideal  $Q$  value ( $1.3 \times 10^{17} \text{ cm}^{-2}$ ) required for the 100% protonation/deprotonation of a- $WO_3$ , according to the following reaction:  $WO_3 + H^+ + e^- \rightleftharpoons HWO_3$  (the  $Q$  is estimated by  $Q = \frac{\rho \times T}{M} \times N_A$ , where  $M$  is molar mass of  $WO_3$ ,  $\rho$  is the film density,  $T$  is the film thickness, and  $N_A$  is Avogadro constant, respectively).

The activation energy ( $E_a$ ) of the electrical conductivity for the fully protonated a- $H_xWO_3$  channel that was determined by  $R_s-T$  measurements (Fig. S1) was  $E_a = 4.3 \times 10^{-3} \text{ eV}$ . This was an order of magnitude smaller than  $E_a = 5.0 \times 10^{-2} \text{ eV}$  reported for the a- $H_xWO_3$  film ( $x = 0.32$ )<sup>27</sup>. Since the  $E_a$  is a function of  $x$  due to the band filling, the much lower  $E_a$  in the a- $WO_3$  channel layer supports that it is effectively protonated by water-electrolysis with high electric-field application in the present TFT-type structure. This result also supports the above conclusion. In addition,  $R_s$  decreased and increased along the universal line under all values of  $V_g$  (Fig. 5c), indicating that all the provided electrons were used for electrochemical protonation/deprotonation of the a- $WO_3$  channel, obeying Faraday's laws of electrolysis, and that the device operation can be controlled by the current density.

The present device with leakage-free water can be reversibly switched from a colorless transparent insulator to a colored metallic conductor in a short amount of time ( $\sim 10$  s, see Video S1). In the ON state, visible light cannot transmit through the device, whereas it can fully transmit in the OFF state. The device can also function as an ON/OFF power switch for other electronic devices. The device is mainly composed of amorphous oxide films, which can be deposited at RT with no substrate heating required. This means there are no limitations on the type of substrate materials that can be used for the device. Moreover, the device can be operated without sealing thanks to the liquid-leakage-free CAN gate insulator. These features are suitable for the development of large-area devices and mass production; thus, the present device may find practical application in future energy-saving technologies, such as advanced smart windows.

In summary, we have demonstrated a liquid-leakage-free transparent EC-MI switching device, which has a three-terminal TFT-type structure consisting of transparent oxide thin films of a- $WO_3$  active channel, CAN gate insulator, NiO/ITO gate electrode, and ITO source-drain electrodes. At initial state, the device was fully transparent in the visible light region and the  $WO_3$  channel was insulator. For  $+V_g$  application, the device became dark-blue-colored state and the  $R_s$  of the  $WO_3$  channel drastically decreased due to the protonation of a- $WO_3$  channel. For  $-V_g$  application, deprotonation of a- $WO_3$  channel occurred and the device returned to colorless-transparent-insulator state. The reversible EC operation (transmission modulation of 35% at  $\lambda$  of 700 nm) and MI switching ( $R_s$ -modulation ratio  $\sim 10^6$ ) were simultaneously demonstrated. The present transparent EC-MI switching device with leakage-free water is composed mostly of amorphous oxide thin films, which can be deposited at RT, and can be operated without sealing. Such low cost device will find the practical application for future energy saving technologies such as advanced smart-windows.

## Methods

**Device fabrication.** The present liquid-leakage-free transparent EC-MI switching device (active channel area:  $400 \mu\text{m}$  in width and  $800 \mu\text{m}$  in length) was fabricated on an alkaline-free glass substrate (Corning® EAGLE XG®, substrate size:  $10 \times 10 \times 0.7 \text{ mm}^3$ ) by pulsed laser deposition (PLD) using stencil masks. All the thin-film fabrication was conducted at RT, where a KrF excimer laser (wavelength of 248 nm, repetition rate of 10 Hz) was used to ablate ceramic target disks. First, 20-nm-thick metallic ITO films were deposited at  $O_2$  pressure ( $P_{O_2}$ ) of 4 Pa as the transparent source and drain electrodes. Then, a- $WO_3$  channel layer was deposited under  $P_{O_2}$  of 7 Pa, where the deposition rate of a- $WO_3$  film was  $6 \text{ nm min}^{-1}$ . 300-nm-thick CAN gate insulator was deposited under  $P_{O_2}$  of 5 Pa to make CAN film nanoporous structure<sup>13,14</sup>. NiO (20 nm)/ITO (20 nm) bilayer film was deposited as the transparent gate electrode on the CAN film surface, where the nanopores in the CAN film is small enough to prevent the NiO/ITO film penetrate into the CAN film and reach a- $WO_3$  layer during the deposition.

**Structural characterization.** Crystallinity of the fabricated thin films were investigated by grazing incidence X-ray diffraction analyses (Cu  $K\alpha_1$ , ATX-G, Rigaku Co.), which revealed that all oxide layers were amorphous in nature expect for NiO polycrystalline film. Cross-sectional thin-film samples for TEM observations were prepared by focused-ion-beam (FIB) micro-sampling technique, in which the multilayer structure region of the TFTs was cutout and thinned by FIB (FB-2000A, HITACHI) to obtain samples for cross-sectional observation. The cross-sectional microstructure and electron diffraction pattern of the a- $WO_3$  devices were examined by high-resolution TEM and STEM (JEM-ARM200F, 200 kV, JEOL Ltd.).

**Electrical and optical property measurements.**  $I_g$  was measured between the gate and source electrodes during the  $V_g$  application using a source measurement unit (Keithley 2450). The electrical and optical properties were measured after switching the  $V_g$  off, because of the non-volatile device operation due to the electrochemical reaction.  $R_s$  were measured by the d.c. four-point probe method (van der Pauw configuration). For the retention time dependence of  $I_g$  and  $R_s$  (Fig. 5a,b),  $I_g$  was measured at 1 s intervals, and  $R_s$  was measured at each interval of 20 s for +3 V, 10 s for +5 V, 5 s for +10 V, 5 s for -3 V, 2 s for -5 V, 1 s for -10 V, respectively. Thermopower ( $S$ ) was measured by giving a temperature difference ( $\Delta T$ ) of  $\sim 4$  K in the film using two Peltier devices, where the actual temperatures of both sides of a- $\text{WO}_3$  channel layer were monitored by two tiny thermocouples. The thermo-electromotive force ( $\Delta V$ ) and  $\Delta T$  were simultaneously measured, and the  $S$ -values were obtained from the linear slope of the  $\Delta V$ - $\Delta T$  plots. Optical transmission spectra were measured by UV-Vis/NIR microscope with the light irradiation area of  $100 \mu\text{m}$  in diameter (MSV-5200, JASCO). The relative humidity value, at which the device operation was tested, was  $\sim 30\%$  at  $25^\circ\text{C}$ . Since the present device electrochemically operates in a cycled process between a- $\text{WO}_3$  cathodic layer ( $\text{WO}_3 + x\text{H}^+ + xe^- \rightarrow \text{H}_x\text{WO}_3$ ) and NiO anodic layer ( $\text{NiO} + \text{OH}^- \rightarrow \text{NiOOH} + e^-$ ), the water in CAN gate insulator should not be lost during the device operation and the CAN does not degrade after many cycles because of the no gas generation. However, it is considered that the humidity in air slightly affect the device operation, which should be tested in the near future.

## References

1. Granqvist, C. G. Electrochromic tungsten oxide films: Review of progress 1993–1998. *Sol. Energy Mater. Sol. Cells* **60**, 201–262 (2000).
2. González-Borrero, P. P. *et al.* Optical band-gap determination of nanostructured  $\text{WO}_3$  film. *Appl. Phys. Lett.* **96**, 061909, doi: 10.1063/1.3313945 (2010).
3. Zheng, H. *et al.* Nanostructured tungsten oxide—properties, synthesis, and applications. *Adv. Funct. Mater.* **21**, 2175–2196 (2011).
4. Dickens, P. G. & Whittingham, M. S. The tungsten bronzes and related compounds. *Q. Rev. Chem. Soc.* **22**, 30–44 (1968).
5. Granqvist, C. G. Oxide electrochromics: Why, how, and whither. *Sol. Energy Mater. Sol. Cells* **92**, 203–208 (2008).
6. Deb, S. K. Opportunities and challenges in science and technology of  $\text{WO}_3$  for electrochromic and related applications. *Sol. Energy Mater. Sol. Cells* **92**, 245–258 (2008).
7. Ohta, H. & Hosono, H. Transparent oxide optoelectronics. *Mater. Today* **7**, 42–51 (2004).
8. Fortunato, E., Barquinha, P. & Martins, R. Oxide semiconductor thin-film transistors: A review of recent advances. *Adv. Mater.* **24**, 2945–2986 (2012).
9. Ahn, C. H. *et al.* Electrostatic modification of novel materials. *Rev. Mod. Phys.* **78**, 1185–1212 (2006).
10. Natan, M. J., Mallouk, T. E. & Wrighton, M. S. The pH-sensitive tungsten(VI) oxide-based microelectrochemical transistors. *J. Phys. Chem.* **91**, 648–654 (1987).
11. Barquinha, P. *et al.* Flexible and transparent  $\text{WO}_3$  transistor with electrical and optical modulation. *Adv. Electron. Mater.* **1**, 1500030, doi: 10.1002/aelm.201500030 (2015).
12. Deb, S. K. Optical and photoelectric properties and colour centres in thin films of tungsten oxide. *Philos. Mag.* **27**, 801–622 (1973).
13. Ohta, H. *et al.* Field-induced water electrolysis switches an oxide semiconductor from an insulator to a metal. *Nature Commun.* **1**, 118, doi: 10.1038/ncomms1112 (2010).
14. Ohta, H. *et al.* Unusually large enhancement of thermopower in an electric field induced two-dimensional electron Gas. *Adv. Mater.* **24**, 740–744 (2012).
15. Vondrák, J. & Bludská, J. The role of water in hydrogen insertion into  $\text{WO}_3$ . *Solid State Ion.* **68**, 317–323 (1994).
16. Xia, X. H. *et al.* Electrochromic properties of porous NiO thin films prepared by a chemical bath deposition. *Sol. Energy Mater. Sol. Cells* **92**, 628–633 (2008).
17. Tanisaki, S. On the phase transition of tungsten trioxide below room temperature. *J. Phys. Soc. Jpn.* **15**, 566–573 (1960).
18. Light, T. S., Licht, S., Bevilacqua, A. C. & Morash, K. R. The fundamental conductivity and resistivity of water. *Electrochem. Solid-State Lett.* **8**, E16–E19 (2005).
19. Katase, T., Endo, K. & Ohta, H. Thermopower analysis of the electronic structure around the metal-insulator transition in  $\text{V}_{1-x}\text{W}_x\text{O}_2$ . *Phys. Rev. B* **90**, 161105, doi: 10.1103/PhysRevB.90.161105 (2014).
20. Katase, T., Endo, K., Tohei, T., Ikuhara, Y. & Ohta, H. Room-temperature-protonation-driven On-demand metal-insulator conversion of a transition metal oxide. *Adv. Electron. Mater.* **1**, 1500063, doi: 10.1002/aelm.201500063 (2015).
21. Vannice, M. A., Boudart, M. & Fripiat, J. J. Mobility of hydrogen in hydrogen tungsten bronze. *J. Catal.* **17**, 359–365 (1970).
22. Xi, Y., Zhang, Q. & Cheng, H. Mechanism of hydrogen spillover on  $\text{WO}_3(001)$  and Formation of  $\text{H}_x\text{WO}_3$  ( $x = 0.125, 0.25, 0.375$ , and  $0.5$ ). *J. Phys. Chem. C* **118**, 494–501 (2014).
23. Zhongkuan, L., Zishang, D. & Zhonghua, J. Electrochromic kinetics of amorphous  $\text{WO}_3$  films. *J. Non-Cryst. Solids* **112**, 309–313 (1989).
24. Granqvist, C. G. *Handbook of Inorganic Electrochromic Materials*, Ch. 19, 339–377 (Elsevier, 1995).
25. Miyakawa, M., Ueda, K. & Hosono, H. Carrier generation in highly oriented  $\text{WO}_3$  films by proton or helium implantation. *J. Appl. Phys.* **92**, 2017–2022 (2002).
26. Crandall, R. S., Wojtowicz, P. J. & Faughnan, B. W. Theory and measurement of the change in chemical potential of hydrogen in amorphous  $\text{H}_x\text{WO}_3$  as a function of the stoichiometric parameter  $x$ . *Solid State Commun.* **18**, 1409–1411 (1976).
27. Crandall, R. S. & Faughnan, B. W. Electronic transport in amorphous  $\text{H}_x\text{WO}_3$ . *Phys. Rev. Lett.* **39**, 232–235 (1977).

## Acknowledgements

The authors thank N. Kawai for experimental help on TEM/STEM analyses. The TEM/STEM analyses, conducted at Hokkaido University, were supported by Nanotechnology Platform Program from MEXT. T.K. was supported by Grant-in-Aid for Young Scientists A (15H05543), for Challenging Exploratory Research (16K14377) from JSPS and a research grant from The Mazda Foundation. H.O. was supported by Grant-in-Aid for Scientific Research on Innovative Areas (25106007), for Scientific Research A (25246023) from JSPS and the Asahi Glass Foundation.

## Author Contributions

T.K., T.O., M.H. and T.M. performed the device fabrication, measurements and data analyses. T.K. performed TEM/STEM analyses. All authors discussed the results and commented on the manuscript. H.O. planned and supervised the project.

## Additional Information

**Supplementary information** accompanies this paper at <http://www.nature.com/srep>

**Competing financial interests:** The authors declare no competing financial interests.

**How to cite this article:** Katase, T. *et al.* A transparent electrochromic metal-insulator switching device with three-terminal transistor geometry. *Sci. Rep.* **6**, 25819; doi: 10.1038/srep25819 (2016).



This work is licensed under a Creative Commons Attribution 4.0 International License. The images or other third party material in this article are included in the article's Creative Commons license, unless indicated otherwise in the credit line; if the material is not included under the Creative Commons license, users will need to obtain permission from the license holder to reproduce the material. To view a copy of this license, visit <http://creativecommons.org/licenses/by/4.0/>